

# UC Davis

## UC Davis Previously Published Works

### Title

Non-invasive quantification of 18F-florbetaben with total-body EXPLORER PET

### Permalink

<https://escholarship.org/uc/item/0444k2xw>

### Journal

EJNMMI Research, 14(1)

### ISSN

2191-219X

### Authors

Holy, Emily Nicole

Li, Elizabeth

Bhattarai, Anjan

et al.

### Publication Date

2024

### DOI

10.1186/s13550-024-01104-7

Peer reviewed

ORIGINAL RESEARCH

Open Access



# Non-invasive quantification of $^{18}\text{F}$ -florbetaben with total-body EXPLORER PET

Emily Nicole Holy<sup>1,2\*</sup> , Elizabeth Li<sup>2</sup>, Anjan Bhattarai<sup>1,2</sup>, Evan Fletcher<sup>1</sup>, Evelyn R. Alfaro<sup>1</sup>, Danielle J. Harvey<sup>4</sup>, Benjamin A. Spencer<sup>2,3</sup>, Simon R. Cherry<sup>2,3</sup>, Charles S. DeCarli<sup>1</sup> and Audrey P. Fan<sup>1,2</sup>

## Abstract

**Background** Kinetic modeling of  $^{18}\text{F}$ -florbetaben provides important quantification of brain amyloid deposition in research and clinical settings but its use is limited by the requirement of arterial blood data for quantitative PET. The total-body EXPLORER PET scanner supports the dynamic acquisition of a full human body simultaneously and permits noninvasive image-derived input functions (IDIFs) as an alternative to arterial blood sampling. This study quantified brain amyloid burden with kinetic modeling, leveraging dynamic  $^{18}\text{F}$ -florbetaben PET in aorta IDIFs and the brain in an elderly cohort.

**Methods**  $^{18}\text{F}$ -florbetaben dynamic PET imaging was performed on the EXPLORER system with tracer injection (300 MBq) in 3 individuals with Alzheimer's disease (AD), 3 with mild cognitive impairment, and 9 healthy controls. Image-derived input functions were extracted from the descending aorta with manual regions of interest based on the first 30 s after injection. Dynamic time-activity curves (TACs) for 110 min were fitted to the two-tissue compartment model (2TCM) using population-based metabolite corrected IDIFs to calculate total and specific distribution volumes ( $V_T$ ,  $V_S$ ) in key brain regions with early amyloid accumulation. Non-displaceable binding potential ( $BP_{ND}$ ) was also calculated from the multi-reference tissue model (MRTM).

**Results** Amyloid-positive (AD) patients showed the highest  $V_T$  and  $V_S$  in anterior cingulate, posterior cingulate, and precuneus, consistent with  $BP_{ND}$  analysis.  $BP_{ND}$  and  $V_T$  from kinetic models were correlated ( $r^2 = 0.46$ ,  $P < 2e^{-16}$ ) with a stronger positive correlation observed in amyloid-positive participants, indicating reliable model fits with the IDIFs.  $V_T$  from 2TCM was highly correlated ( $r^2 = 0.65$ ,  $P < 2e^{-16}$ ) with Logan graphical  $V_T$  estimation.

**Conclusion** Non-invasive quantification of amyloid binding from total-body  $^{18}\text{F}$ -florbetaben PET data is feasible using aorta IDIFs with high agreement between kinetic distribution volume parameters compared to  $BP_{ND}$  in amyloid-positive and amyloid-negative older individuals.

**Keywords**  $^{18}\text{F}$ -florbetaben, Alzheimer disease,  $\beta$ -Amyloid, Total body EXPLORER PET, Kinetic modeling, image derived input function

\*Correspondence:

Emily Nicole Holy  
enholy@ucdavis.edu

<sup>1</sup>Department of Neurology, University of California (UC) Davis Health,  
1590 Drew Avenue, Davis, CA 95618, USA

<sup>2</sup>Department of Biomedical Engineering, UC Davis, Davis, USA

<sup>3</sup>Department of Radiology, UC Davis Health, Davis, USA

<sup>4</sup>Department of Public Health Sciences, UC Davis Health, Davis, USA



© The Author(s) 2024. **Open Access** This article is licensed under a Creative Commons Attribution 4.0 International License, which permits use, sharing, adaptation, distribution and reproduction in any medium or format, as long as you give appropriate credit to the original author(s) and the source, provide a link to the Creative Commons licence, and indicate if changes were made. The images or other third party material in this article are included in the article's Creative Commons licence, unless indicated otherwise in a credit line to the material. If material is not included in the article's Creative Commons licence and your intended use is not permitted by statutory regulation or exceeds the permitted use, you will need to obtain permission directly from the copyright holder. To view a copy of this licence, visit <http://creativecommons.org/licenses/by/4.0/>.

## Introduction

Amyloid imaging with PET radiotracers has proven useful for clinical assessment of Alzheimer's disease and monitoring of response to recently developed anti-amyloid therapies [1, 2]. Typical PET assessment of amyloid is either based on a clinical read (amyloid positive or negative); or quantifies standardized uptake value ratio (SUVR) with reference to a predetermined reference region [3, 4]. However, SUVR does not consider potential confounding variables such as blood volume, tracer metabolism, blood flow, and other pharmacokinetic components representative of tracer dynamics. Furthermore, dynamic PET information of amyloid uptake reveals additional, complementary physiological information at various uptake times, e.g., with early-phase images reflective of tracer delivery via cerebral blood flow and late-phase images reflective of equilibrium amyloid binding [5, 6].

Kinetic model-based approaches are a quantitative alternative to SUVR that characterize distinct tracer dynamics (e.g., blood flow) and account for various physiological processes. Current amyloid tracers such as  $^{18}\text{F}$ -florbetaben, a second-generation amyloid tracer with more specific binding and less off-target binding relative to the first generations, (such as  $^{18}\text{F}$ -DDNP). Although similar binding affinity is observed in  $^{11}\text{C}$ -PiB and  $^{18}\text{F}$ -florbetaben (Sabri et al., Figure 2), the half lives are 20 min and 110 min, respectively. The longer half-life of  $^{18}\text{F}$  allows for greater distribution radius therefore increasing its availability [2, 7].  $^{18}\text{F}$ -florbetaben is typically modeled with two tissue compartments. Due to florbetaben's reversibly binding nature, the tissue-to-plasma equilibrium ratio not only reflects the available specific binding site density but also free and nonspecific binding of tracer [8]. Non-displaceable binding potential ( $BP_{ND}$ ) is a typical measurement from reference tissue methods and can be measured without arterial plasma measurements and it describes the ratio at equilibrium of specifically bound tracer to that of non-displaceable radioligand in tissue.  $BP_{ND}$  measurements from dynamic PET also benefit from being less sensitive to changes in cerebral blood flow (CBF) and noise related to SUVR such as tracer clearance, blood flow, blood volume, and/or extraction fraction [9]. On the other hand, full compartment modeling with a two-tissue model directly estimates specific rate constants such as  $K_1$ , which reflects both tracer delivery (perfusion) and extraction fraction,  $k_3$  reflecting metabolism or binding, clearance from the tissue back to the blood ( $k_2$ ,  $k_4$ ), and blood volume ( $V_b$ ). Additionally, parameters more directly related to receptor binding density can be calculated, including the total ( $V_T$ ) and specific distribution volumes ( $V_S$ ) [10]. While binding potential and the volume of distribution measures are expected to correlate [8], the kinetic rate

parameters estimated from two-tissue compartment modeling add further insight into specific underlying processes that govern amyloid PET uptake over time.

However, one disadvantage of full kinetic modeling is the requirement of an arterial blood input function, which is typically measured through multiple arterial blood samples during the PET scan. Arterial cannulation blood sampling is invasive, potentially painful, time consuming, and often discourages patients from participating in clinical research involving dynamic PET imaging. Sampling errors can also occur, and the arterial input function needs to be "low-noise" to avoid error propagation to kinetic estimates [11]. In addition, there is an inherent tradeoff between spatial and temporal resolution to achieve adequate signal-to-noise of dynamic PET frames for robust kinetic parameter fits [12, 13]. Using conventional PET scanners with  $\sim 20$  cm field of view (FOV) only a limited FOV of continuous dynamic data is available and will suffer from multiple gaps in time if an image-derived input function (IDIF) is used. The uEXPLORER total-body PET system reduces these tradeoffs and allows for the acquisition of IDIFs from vessels and arteries in the body at early time frames to be used as a surrogate for arterial blood sampling while simultaneously acquiring dynamic brain activity. Moreover, the high sensitivity of the uEXPLORER scanner allows for fast temporal sampling, i.e., 2-second frames especially at early time points, while maintaining high image resolution, thus overcoming previous challenges with IDIF methods [12, 14].

The purpose of this study is to leverage the total-body EXPLORER scanner to extract reliable IDIFs from the descending aorta and apply a kinetic modeling-based approach to quantify brain  $\beta$ -Amyloid in an elderly cohort. We used non-invasive two-tissue compartment modeling to quantify  $V_T$  and  $V_S$  across brain regions and evaluated them with  $BP_{ND}$  values derived from a reference tissue-based model. Additionally, microparameters ( $K_1$ ,  $k_2$ ,  $k_3$ , and  $k_4$ ) were derived and evaluated. Furthermore, we expected to see that regional measures of  $V_T$  and  $V_S$  from kinetic modeling are elevated in "index" brain regions that has previously been shown to accumulate amyloid in amyloid-positive versus amyloid-negative individuals [15].

## Materials and methods

### Subjects

We recruited 15 participants, including 3 participants with Alzheimer's Disease (AD,  $75.7 \pm 4.6$  years), 3 with mild cognitive impairment (MCI,  $84.5 \pm 10.6$  years), and 9 healthy controls (HC,  $77.2 \pm 6.0$  years) from the UC Davis Alzheimer's Disease Research Center cohort. All

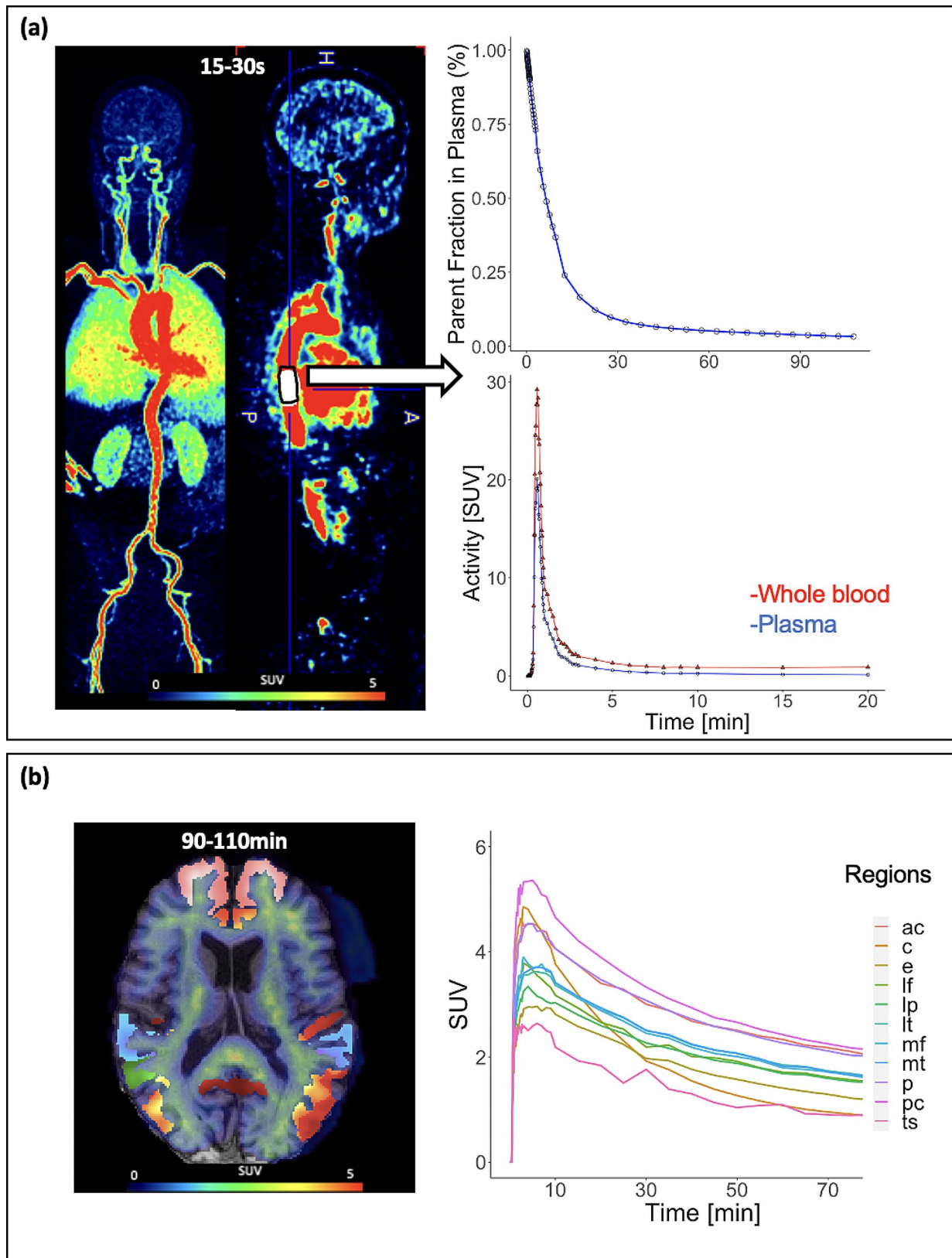


**Fig. 1** Dynamic total-body  $^{18}\text{F}$ -florbetaben data. **(A)** Literature-based metabolite fraction curve [21] (top), dynamic PET aorta image-derived input function representing whole blood (red) and plasma (blue) (middle). **(B)** Brain tissue time-activity curves (right) for a 73-year-old male with Alzheimer's Disease. Anterior cingulate (ac), cerebellar gray matter (c), entorhinal cortex (e), lateral frontal cortex (lf), lateral parietal cortex (lp), lateral temporal cortex (lt), medial frontal cortex (mf), medial temporal cortex (mt), precuneus (p), posterior cingulate (pc), and temporal sulci (ts)

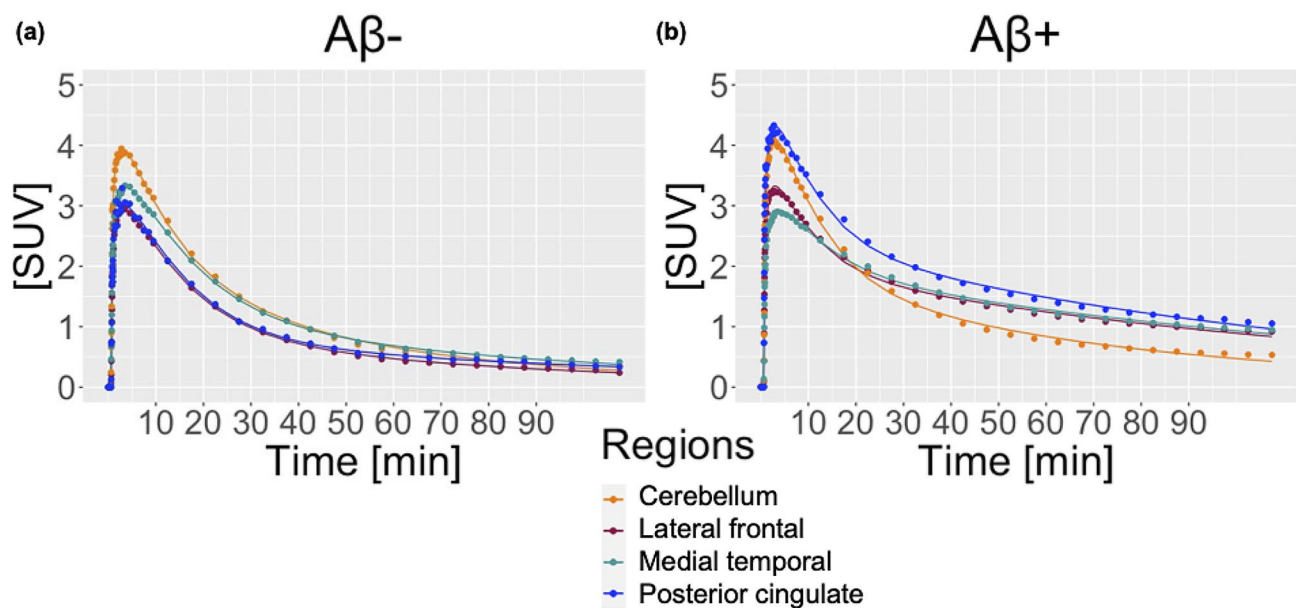


**Fig. 2** Two-tissue compartment model fits to measured time-activity curves for lateral frontal cortex, medial temporal cortex, posterior cingulate, and cerebellar gray matter in (A) 82-year-old male, cognitively normal participant and (B) 81-year-old male patient with Alzheimer's disease. IDIFs from the aorta were corrected for population-based metabolite fraction and plasma fraction

3 AD patients were amyloid-positive ( $A\beta+$ ), and all HC and MCI individuals were amyloid-negative ( $A\beta-$ ), resulting in 3 amyloid-positive cases and 12 amyloid-negative cases. Eligibility criteria included: age over 65 years, able to undergo an MRI, and known cognitive status based on clinical assessment and neuropsychological testing. Individuals with pacemakers, brain tumors, alcoholism and/or those who were not able to lie still for 90 min were excluded from this study. The UC Davis Institutional Review Board approved this protocol and written informed consent was obtained for all subjects involved in the study.

#### PET and MRI acquisition

##### Amyloid-PET

PET data were acquired with the UC Davis total-body uEXPLORER PET scanner [13, 16].  $^{18}\text{F}$ -florbetaben was administered to 15 participants via bolus injection with an average dose of  $277.1 \pm 22.4$  MBq. An ultra-low dose CT was obtained for anatomic localization and attenuation correction purposes immediately before the dynamic PET acquisition. The 140 kVp ultra-low dose CT had a tube current of  $\sim 5$  mAs with automatic dose modulation, leading to an estimated dose of 1 mSv per acquisition. CT images were reconstructed into a  $1024 \times 1024$  matrix with a 2.344 mm slice thickness and 512 mm axial FOV. Dynamic PET data were acquired over 110 min and reconstructed into  $30 \times 2$ -second frames,  $12 \times 10$ -second frames,  $7 \times 1$ -minute frames, and  $20 \times 10$ -minute frames following a high-temporal resolution total-body PET protocol established previously [17]. All image data were

reconstructed using time-of-flight based ordered-subset expectation-maximization (OSEM) with all standard corrections but without point spread function modeling. Four OSEM iterations of 20 subsets were employed. Images.

were reconstructed with a 2.344 mm isotropic voxel size and without post-reconstruction smoothing following the UC Davis clinical protocol [18].

Amyloid positivity was determined by a clinical read on static PET scans by a trained neurologist (C.D.) with over 30 years of experience and certified to clinically determine PET amyloid positivity.

##### MRI

All participants underwent MRI scans on a 3 Tesla Siemens Tim Trio whole-body scanner equipped with a 32-channel head coil. The scanning parameters of the T1-weighted 3D magnetization-prepared rapid gradient-echo (MPRAGE) sequence included: matrix size= $240 \times 256$ , in-plane spatial resolution=1 mm, repetition time=2300 ms, echo time=2.98 ms, flip angle=9 degrees, acquisition time=9 min 14 s, inversion time=900–1100 s, and 176 sagittal slices with thickness=1.0–1.2 mm. PET and MRI scans were taken on average  $2.5 \pm 1.5$  years apart from each other.

##### Image-derived input function

15 hand-drawn IDIFs were manually extracted in PMOD (PMOD Technologies, LLC) from the descending aorta from an early time window (mean initial frame  $25.3 \pm 6.9$  s, mean volume= $19.4 \pm 5.2$  cm<sup>3</sup>) (Fig. 1). The



IDIF region of interest (ROI) length was kept consistent across all individuals and was 18–20 voxels in the superior-inferior direction. IDIF ROI diameters varied to align with individual aorta anatomy but were eroded by 1 mm in all dimensions to avoid including the vessel walls. To completely avoid blood sampling, the IDIF was corrected for metabolite and plasma fractions using population-based curves from the literature prior to kinetic modeling. Plasma correction was applied by multiplying by a constant value of 0.73 for the whole blood: plasma ratio [19]. A bi-exponential function describing the fraction of unmetabolized  $^{18}\text{F}$ -florbetaben over time was then applied for metabolite correction derived from a previous study consisting of 10 patients with AD and 10 aged matched HCs [20].

### Dynamic processing

The dynamic PET data for each individual underwent brain extraction using PMOD and the FMRIB Software Library (FSL) brain extraction tool [22]. Dynamic PET motion correction was first performed frame by frame to an average image using FSL's MCFLIRT, and linear (affine) registration was performed to align the 4D motion-corrected dynamic PET data with their respective T1-weighted (T1W) images using FSL's FLIRT [23, 24].

Using the Desikan-Killiany-Tourville (DKT) atlas, brain regions of interest that are known to accumulate amyloid were placed in the 10 following index regions: lateral frontal cortex (LF), medial frontal cortex (MF), anterior cingulate (AC), posterior cingulate (PC), lateral temporal cortex (LT), lateral parietal cortex (LP), medial temporal cortex (MT), entorhinal cortex (E), temporal sulci (TS), and the precuneus (P) by combining several subregions based on literature [3, 25], (Supplemental Fig. 1). These ROIs were obtained using subject-specific T1-weighted image segmentation with in-house software [25]. Time-activity curves were extracted from each of the brain regions and expressed as standardized uptake value (SUV, Fig. 1b). The cerebellar grey matter ROI was segmented using the DKT atlas described above for reference tissue-based modeling and for SUVR calculation.

### Kinetic modeling

Kinetic modeling of regional time-activity curves was performed both using the 2-tissue compartment model (2TCM) and Logan graphical analysis. Kinetic modeling was performed using in-house software and specific methods used for quantification are described in detail in the literature [17, 20]. For the 2TCM, delay between the aorta IDIF and brain time-activity curves (TACs) was calculated using joint estimation using all 69 reconstructed timepoints [26]. Results were obtained using a nonlinear

least-squares fitting process. Initialization parameters are described in Supplemental Table 1.

$$V_s = \frac{K_1 k_3}{k_2 k_4} \quad (1)$$

$$V_T = \frac{K_1}{k_2} \left(1 + \frac{k_3}{k_4}\right) \quad (2)$$

2TCM kinetic parameters such as,  $V_b$ ,  $K_1$ ,  $k_2$ ,  $k_3$ ,  $k_4$ , specific distribution volume ( $V_s$ , Eq. 1), and total distribution volume ( $V_T$ , Eq. 2) were extracted independently for all 10 brain regions.  $V_b$  represents blood volume.  $K_1$  (mL/min/cm<sup>3</sup>) describes tracer transport from arterial plasma into the first tissue compartment, while  $k_2$  (1/min) describes transport from the first tissue compartment back into the blood pool. The  $k_3$  and  $k_4$  rate parameters (units 1/min) describe forward and backward transport, respectively, of the tracer between the two tissue compartments.

$$\text{Logan}V_T = \frac{\int_0^t C_T(t) dt}{C_T(t)} = V_T \frac{\int_0^t C_P(t) dt}{C_T(t)} + \text{Int} \quad (3)$$

Logan graphical analysis was also performed to estimate total distribution volume ( $V_T$ , Eq. 3) in MATLAB (version 2020a), using the image-based input function  $C_P(t)$  and the brain time-activity curve,  $C_T(t)$ , for each ROI [18].  $t^*$  was set to 30 min and  $V_T$  was calculated separately for each brain region.

$$BP_{ND} = DVR - 1 = \frac{(V_T - V_{ND})}{V_{ND}} \quad (4)$$

Multilinear reference tissue modeling (MRTM) was performed to quantify non-displaceable binding potential using cerebellar grey as the reference.  $V_{ND}$  represents the distribution volume of nondisplaceable compartment relative to total concentration of tracer in plasma.  $t^*$  was set to 30 min. ( $BP_{ND}$ , Eq. 4).

### Statistical analysis

Because measurements of the outcomes of interest ( $V_T$ ,  $V_s$ ,  $BP_{ND}$ , and  $K_1$ ) were available in several brain regions for each person, linear mixed effects models were used to understand how amyloid status and brain regions were associated with outcomes, including a person-specific random effect to account for multiple regions within a person. Separate models were fit for each outcome measure. Similar linear mixed effects models were also used to describe the effect of amyloid status on each kinetic rate parameter. Exploratory analysis was performed to investigate any driving microparameters behind  $V_T$  and  $V_s$  outcome measures using the same principles of the

linear mixed effects models described above. Benjamini-Hochberg False discovery rate (FDR) was applied to correct for multiple comparisons when reporting *p*-values [27]. To assess the correlation between  $V_T$ ,  $V_S$ , and SUVR with  $BP_{ND}$ ,  $V_T$ ,  $V_S$ ,  $BP_{ND}$ , and SUVR with  $K_1$ , as well as to correlate  $V_T$  measures from the two-tissue compartment model versus Logan analysis, all measurements across regions were included. For these correlations, a linear mixed effects model was again used with a person-specific random effect, although in these models, brain region was not of specific interest and therefore not included as a variable in the model. All analyses were conducted using RStudio and a significance level of 0.05 was used [28].

**Results**

**Compartment models**

High quality fits of  $\beta$ -Amyloid binding were achieved through the 2TCM model with the corrected IDIF and accounting for time delay through joint estimation. Typical time-activity curves for 1 HC/ $A\beta^-$  and 1 patient with AD/ $A\beta^+$  are shown in Fig. 2, revealing good model fits to our data. In the  $A\beta^-$  individual, the lateral frontal, medial temporal and posterior cingulate showed similar TAC patterns as the cerebellar gray. The signal reached peaks (~3–4 SUV) for all regions and revealed no regional separation over later time points. In the  $A\beta^+$  patient, TAC peaks during the early time point were similar (~3–4 SUV) across all regions; however, unlike the  $A\beta^-$  case, brain index regions showed higher SUV compared to cerebellar gray over time, especially after 30 min.

**Kinetic modeling quantification**

$BP_{ND}$  was elevated across regions in  $A\beta^+$  participants ( $2.47 \pm 0.28$ ) compared to  $A\beta^-$  participants ( $1.14 \pm 0.17$ ), which agreed with the visual clinical assessment. Similar average elevations in  $V_S$  ( $A\beta^+ = 11.36 \pm 3.05$ ;  $A\beta^- = 6.48 \pm 2.26$ ) and  $V_T$  ( $A\beta^+ = 18.04 \pm 3.44$ ;  $A\beta^- = 12.24 \pm 3.01$ ) were observed from 2TCM fitting (Fig. 3). Figure 3 reports the significant difference between  $A\beta^+$  and  $A\beta^-$  groups within each region from mixed-effects modeling (i.e., where the region serves as its own reference in each interaction of the model). After applying this linear mixed-effects model to consider the interaction effect between amyloid status and brain region, FDR analysis revealed that the  $A\beta^+$  group had significantly higher  $V_T$  and  $V_S$  in all index regions, except for the cerebellum, entorhinal cortex, lateral parietal, and temporal sulci (\*\*  $P < 0.0001$ , \*\*\*  $P < 0.001$ , \*\*  $P < 0.01$ , \*  $P < 0.05$ , NS = not significant).  $BP_{ND}$  shows less discriminability and has fewer brain regions that were significantly higher for the  $A\beta^+$  group. Multiple significant interactions between regions were also observed in all measures. The anterior cingulate and posterior cingulate showed the highest discrimination between amyloid positive and amyloid negative groups in all measures.

Table 1 lists kinetic rate parameters estimated by the 2TCM from three example cortical regions (lateral frontal, medial temporal and posterior cingulate) and the cerebellar gray reference from the  $A\beta^+$  and  $A\beta^-$  groups. Identical but separate mixed effects models were used to describe statistical differences in  $V_T$ ,  $V_S$ , and rate parameters.  $K_1$ ,  $k_2$ ,  $k_3$ ,  $k_4$ , delay, and blood volume parameters values revealed no significant differences between the

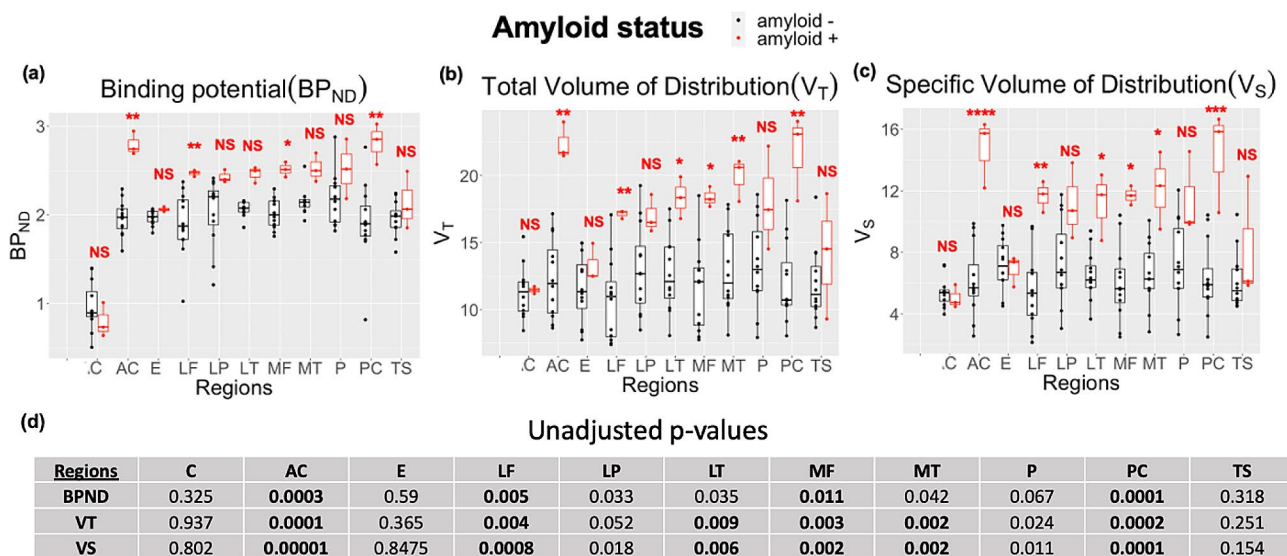


**Fig. 3** Regional  $BP_{ND}$ (A),  $V_T$ (B), and  $V_S$ (C) values for cortical regions: anterior cingulate (AC), entorhinal (E), lateral frontal (LF), lateral parietal (LP), lateral temporal (LT), medial frontal (MF), medial temporal (MT), precuneus (P), posterior cingulate (PC), temporal sulci (TS), and for cerebellar reference region (C). Amyloid-positive individuals showed the highest values in all three parameters compared to amyloid-negative cohorts in relation to the interquartile range. Unadjusted *p*-values for all brain regions where bold indicates significance above the threshold (D)

**Table 1** Kinetic Parameter Values

Regions	Aβ+(n=3)				Aβ- (n=12)			
	Index Regions			Reference	Index Regions			Reference
	LF	MT	PC	C	LF	MT	PC	C
$K_1$ (mL.cm <sup>-3</sup> .min <sup>-1</sup> )	0.404±0.087	0.44±0.180	0.5±0.065	0.498±0.097	0.480±0.083	0.505±0.071	0.570±0.082	0.629±0.065
$k_2$ (min <sup>-1</sup> )	0.076±0.023	0.059±0.034	0.069±0.018	0.078±0.021	0.094±0.02	0.082±0.018	0.102±0.021	0.112±0.027
$k_3$ (min <sup>-1</sup> )	0.032±0.008	0.023±0.014	0.036±0.011	0.012±0.006	0.019±0.008	0.022±0.011	0.021±0.008	0.044±0.043
$k_4$ (min <sup>-1</sup> )	0.018±0.002	0.014±0.003	0.018±0.0009	0.024±0.003	0.019±0.005	0.023±0.019	0.021±0.009	0.042±0.028
$V_T$ (cortex)	<b>17.126 ± 0.300</b>	<b>19.905 ± 1.607</b>	<b>21.737 ± 3.181</b>	11.467±0.268	10.761±3.098	12.941±3.110	12.071±3.033	11.328±1.941
$V_T$ (cerebellum) (mL.cm <sup>-3</sup> )	* †	* †	* †					
$V_s = "K_1.k_3" / "k_2.k_4"$ (mL.cm <sup>-3</sup> )	<b>11.661 ± 1.010</b>	<b>12.118 ± 2.513</b>	<b>14.360 ± 3.297</b>	5.038±0.757	5.481±2.405	6.508±2.078	6.332±2.402	5.403±0.965
$V_b$ ( $\frac{mL}{mL}$ )	0.040 ± 0.016	0.049±0.037	0.052±0.017	0.052±0.017	0.042 ± 0.014	0.044±0.011	0.056±0.012	0.057±0.018
Delay (s)	6.333 ± 1.528	6 ± 1	6.667 ± 1.528	7 ± 1	5.417 ± 1.730	5.417 ± 1.621	5.417 ± 1.929	6.083 ± 1.165

Significance was found for the following:

\*For  $V_T$  and  $V_s$  Aβ+ index regions were significantly higher than Aβ- index regions \* $p < 0.05$

† Within the Aβ+ group index regions were significantly higher than cerebellar reference \* $p < 0.05$

two amyloid status groups. No significant difference was observed in  $V_s$  or  $V_T$  for the cerebellar cortex between the Aβ+ and Aβ- groups as expected, indicating it is an appropriate reference. However, the Aβ+ showed significantly higher  $V_T$  and  $V_s$  values in all three index regions compared to Aβ- ( $P < 0.05$ ). Considering intra-group comparisons, within the Aβ+ group,  $V_T$  and  $V_s$  in all index regions were significantly higher than the same measures in cerebellar gray ( $P < 0.05$ ), while no significant difference was observed between regions within the Aβ- group.

Table 1. Parameter values from Aβ+ and Aβ- individuals who underwent dynamic <sup>18</sup>F-Florbetaben studies and subsequent kinetic modeling. AD individuals are included in the Aβ+ columns and both MCI and HC individuals are in Aβ- columns. The cortical.

areas or index regions were included due to their involvement in early Braak staging.

These include the lateral frontal cortex (LF), medial temporal cortex (MT), and posterior cingulate (PC), with cerebellar gray matter (C) as the reference.

Perfusion differences in amyloid positive and amyloid negative individuals were not evident in the three index regions chosen for Table 1 but are highlighted in Fig. 4. Only the entorhinal cortex and temporal sulci had significantly lower perfusion in the amyloid positive compared to amyloid negative (entorhinal: \* $P < 0.05$ ), temporal sulci: \*\*\* $P < 0.001$ ). Perfusion was lower in all other brain regions in the amyloid positive group but was not significant. Additionally, when considering a composite of all brain index regions there was a significant difference in perfusion between amyloid positive and amyloid negative groups (\* $P < 0.05$ ).

### Regression modeling of Model parameters: comparison of amyloid binding parameters

Both  $V_s$  ( $P < 2e^{-16}$ ) and  $V_T$  ( $P < 2e^{-16}$ ) were highly correlated with  $BP_{ND}$  across participants (Fig. 5). SUVR correlated with  $V_T$  and  $V_s$ , however as shown in Supplemental Fig. 2, SUVR reflects increased variability and overestimation for amyloid-positive individuals in red compared to amyloid-negative individuals in black. In comparison, this overestimation is not observed in our kinetic measures as seen in Fig. 5.  $V_T$ ,  $V_s$ , and  $BP_{ND}$  had no correlations ( $P > 0.05$ ) with  $K_1$  across all participants and SUVR correlated with  $K_1$  ( $P < 0.05$ ) (Supplemental Figs. 3, 4). Separate  $K_1$  model statistics for the Aβ+ group and Aβ- group showed slight correlation with  $V_T$  (Aβ+:  $P = 0.05$ , Aβ-:  $P = 7.8e^{-6}$ ),  $V_s$  (Aβ+:  $P = 0.04$ , Aβ-:  $P = 1.9e^{-5}$ ), and  $BP_{ND}$  (Aβ+:  $P = 0.04$ , Aβ-:  $P = 0.01$ ). Similarly, no correlation was observed between both  $V_T$  and  $V_s$  with the other microparameters ( $k_2, k_3, k_4$ ).  $V_T$  from Logan analysis was directly compared to  $V_T$  from the 2TCM, with both measures using the same aorta IDIF as input (Fig. 6). Logan  $V_T$  was highly correlated with 2TCM  $V_T$  across brain regions ( $r^2 = 0.65$ ,  $P < 2e^{-16}$ ).

### Discussion

In this paper, we evaluated the feasibility of non-invasive amyloid quantification using kinetic modeling and aorta-based IDIFs with total-body <sup>18</sup>F-florbetaben dynamic PET. Aβ+ individuals showed elevation compared to Aβ- individuals in index brain regions for  $BP_{ND}$ ,  $V_s$ , and  $V_T$  measures. Compartment modeling parameters derived from IDIFs were highly correlated with non-displaceable binding potential ( $BP_{ND}$ ) derived from the multi-reference tissue model, demonstrating quantitative discrimination between Aβ+ and Aβ- participants while contributing additional information about individual



## Tracer Delivery ( $K_1$ )

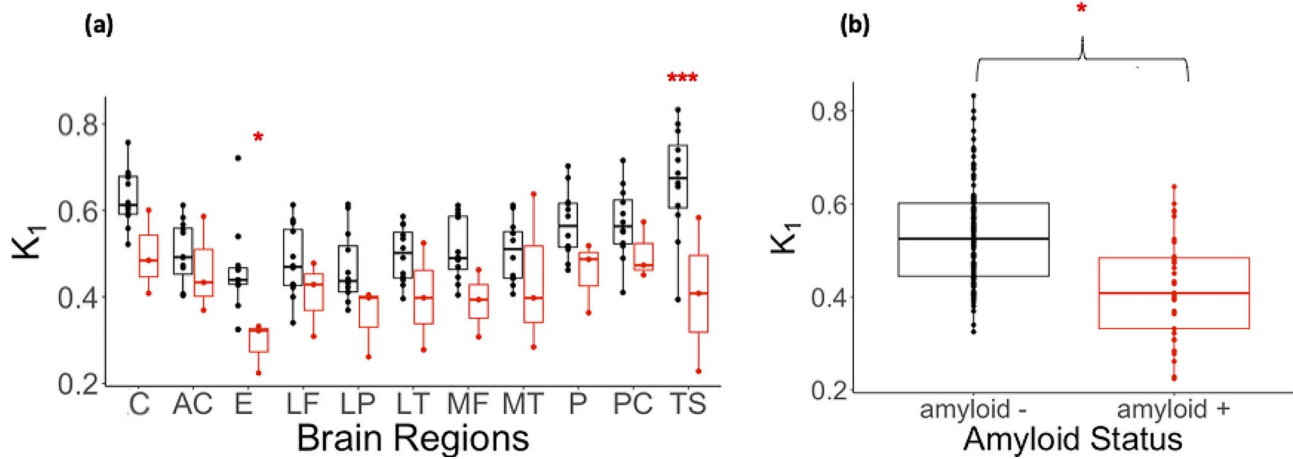


**Fig. 4** (A) Regional  $K_1$  values for cortical regions: anterior cingulate (AC), entorhinal (E), lateral frontal (LF), lateral parietal (LP), lateral temporal (LT), medial frontal (MF), medial temporal (MT), precuneus (P), posterior cingulate (PC), temporal sulci (TS), and for cerebellar reference region (C). Amyloid-positive individuals showed significantly lower perfusion in all entorhinal ( $P=0.01$ ) and temporal sulci ( $P=0.0005$ ) compared to amyloid-negative cohorts. (B) Regional  $K_1$  values for composite of cortical index regions excluding the cerebellar reference region. Amyloid-positive individuals showed significantly higher perfusion compared to amyloid-negative ( $P=0.0283$ )

## $\beta$ -Amyloid binding Characteristics in All Brain Regions

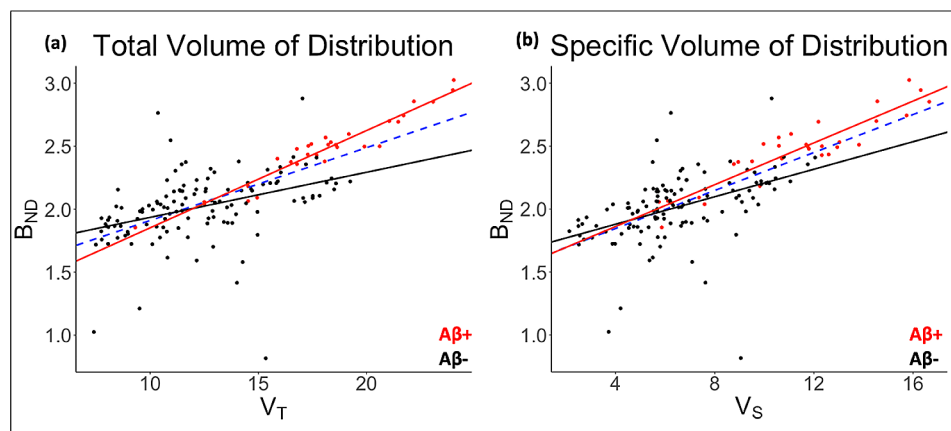


**Fig. 5** Linear regression analysis results accounting for subject clustering for A $\beta$  (red), A $\beta$ - (black), and all subjects (blue dashed). The following model statistics are for all subjects. (A)  $V_T$  and  $B_{ND}$ , ( $r^2 = 0.46, P < 2e^{-16}$ ). (B)  $V_S$  and  $B_{ND}$ , ( $r^2 = 0.51, P < 2e^{-16}$ )

kinetic rate outcome parameters and macroparameters ( $V_T$  and  $V_S$ ).

Through kinetic modeling, we achieved  $V_T$  and  $V_S$  values that were comparable to Becker et al. and were able to quantify differences between amyloid positive versus amyloid negative cases [20]. In addition to significant differences between A $\beta$ + and A $\beta$ - for  $V_T$  and  $V_S$  values across index regions, significant interactions were

also identified, suggesting that the differences in these values between A $\beta$ + and A $\beta$ - varied by region. The general pattern of differences across regions was similar.

across all measures ( $B_{ND}$ ,  $V_T$ , and  $V_S$ ).  $B_{ND}$  showed less discriminability between the A $\beta$ + and A $\beta$ - groups. This may be due to the fact that it was derived from a

reference tissue model (MRTM) versus kinetic modeling, however the general trend remains the same as expected. Of note, the anterior cingulate, posterior cingulate, and precuneus had the highest signal and most significant discrimination between the two groups (A $\beta$ + versus A $\beta$ -) that persisted across all three measures of tracer distribution. This observation is consistent with the regions' key role in the default mode network which has been shown to have early accumulation of amyloid [29].

Quantification of distribution volumes and separate kinetic rate parameters has the potential to better characterize amyloid burden and provides more information about tracer distribution [20].  $V_T$  and  $V_S$  values quantify amyloid binding density with from rate parameters with

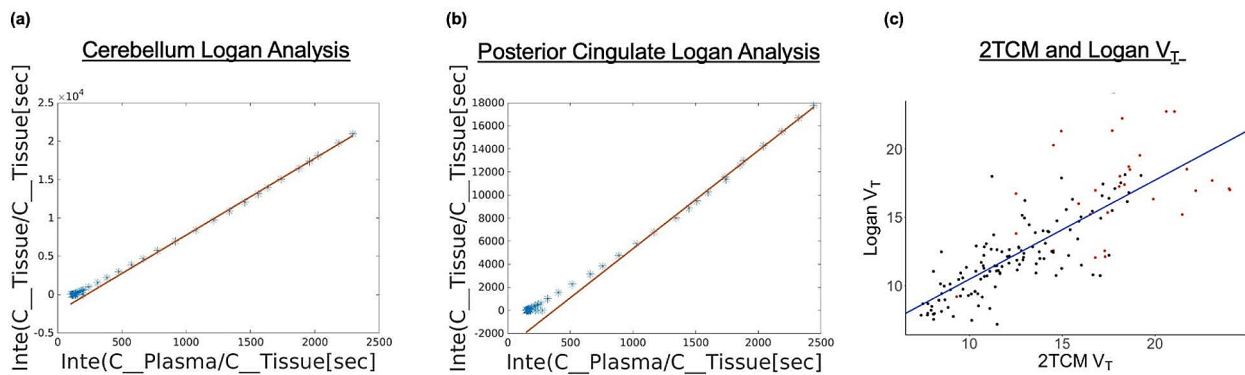


**Fig. 6** Examples of logan graphical analysis for one subject in the cerebellar reference region **(A)** and the Posterior Cingulate **(B)**. **(C)** Correlation between two-tissue compartment model and Logan analysis results for  $V_T$ , accounting for subject clustering.  $V_T$  [2TCM] and  $V_T$  [Logan], ( $r^2 = 0.65$ ).  $V_T$  [Logan] =  $0.73 V_T$  [2TCM] + 3.15

absolute units, and our average model values (Frontal cortex:  $V_S$ :  $A\beta^+ = 11.66$ ;  $A\beta^- = 5.48$ ;  $V_T$ :  $A\beta^+ = 17.13$ ;  $A\beta^- = 10.76$ ; Cerebellum:  $V_T$ :  $A\beta^+ = 11.47$ ;  $A\beta^- = 11.32$ ) were consistent with Becker et al. Table 1 (Frontal cortex:  $V_S$ :  $A\beta^+ = 5.85$ ;  $A\beta^- = 1.86$ ;  $V_T$ :  $A\beta^+ = 13.7$ ;  $A\beta^- = 7.22$ ; Cerebellum:  $V_T$ :  $A\beta^+ = 7.85$ ;  $A\beta^- = 5.36$ ) [20].

From mixed-effects modeling of the parameter values in Table 1, no single kinetic rate parameter that explained the differences in  $V_S$  and  $V_T$  between  $A\beta^+$  and  $A\beta^-$  groups was found. In particular,  $V_S$  and  $V_T$  did not correlate with  $K_1$  across all participants (Supplemental Fig. 4) in this cross-sectional study, which suggests that those measures were not heavily influenced by perfusion-related tracer delivery to specific brain regions. In contrast, we observed a negative correlation of  $K_1$  with SUVR (Supplemental Fig. 3). This could be because perfusion is adding noise and biological variation to SUVR quantification compared to the modeling techniques. However, some differences were observed when considering interactions between kinetic rate parameters, which may reflect their relationships in Eqs. 1 and 2. Additionally, whole body dynamic  $^{18}\text{F}$ -florbetaben PET can give insight to possible perfusion differences in amyloid positive and amyloid negative individuals. Perfusion was significantly lower in brain index regions (composite) in amyloid positive compared to amyloid negative ( $P < 0.05$ ) (Fig. 4). When considering all brain regions separately similar to Fig. 3, significance was only observed in the temporal sulci and entorhinal cortex. We propose, our non-invasive quantification of multiple kinetic parameters could be combined with longitudinal follow-up in future studies to investigate these complex relationships along with disease progression between amyloid buildup and specific processes (e.g., reduced perfusion) in patients with cognitive decline [30].

SUVR has the tendency to overestimate compared to quantitative parameters (e.g.,  $V_T$  and  $V_S$ ), which we

measured using image-derived input functions. Compared to SUVR, compartment modeling of amyloid enables estimation of total distribution volume without assuming a pseudo-equilibrium, and thus is likely more reliable across variable scan durations and amyloid loads. Because it reflects pseudo-equilibrium of  $^{18}\text{F}$ -florbetaben as a reversibly binding tracer, SUVR can slightly overestimate model-based values especially for amyloid-positive individuals [20]. As shown in Supplemental Fig. 2, SUVR reflects increased variability and overestimation for amyloid-positive individuals in red compared to amyloid-negative individuals in black. As an alternative, incorporating a balance between model complexity and quantitative amyloid characterization may be preferred and is possible with Logan graphical analysis. We demonstrated high correlation between  $V_T$  from Logan analysis and 2TCM using the IDIF similar to Su et al., suggesting that Logan-based  $V_T$  is a suitable quantitative measure without extensive computational modeling [31]. The variations in  $V_T$  and  $V_S$  across our amyloid-negative control group may reflect true inter-individual biological variations, which may not be reflected in SUVR values. These variations should be investigated further in future studies alongside a larger cohort of amyloid-positive individuals.

One of the major foci of our study was to assess the feasibility of using a descending aorta IDIF as the input function for compartment modeling. Carotid arteries present an advantage when considering delay due to their proximity to brain tissues, however, are subject to major partial volume effects due to their size [14]. A comparison in our patients was not performed due to the availability of this comparison on the same EXPLORER system with a different tracer and similar reconstruction parameters as described in Li et al. 2019 [32]. Recent work with total-body FDG EXPLORER PET further demonstrated that larger blood pools such as the aorta are more appropriate for 2TCM kinetic estimate compared to

partial volume-limited carotid IDIF [32]. The aortic arch was not chosen due to the complex flow because of connecting arteries and greater cardiac motion that may have influenced modeling of tracer delivery [33]. Using the ascending portion compared to the descending portion of the aorta provided similar IDIF curves, however the descending portion typically demonstrated less curvature and was more easily visible for manual drawing in the sagittal slice. Variability in our IDIF peak and spread may have had some effect on  $K_1$  and  $k_2$  components during modeling and could reflect varying bolus volumes across participants. Our  $K_1$  was slightly higher than Becker et al. (0.2–0.25 vs. 0.3–0.51  $mL \cdot cm^{-3} \cdot min^{-1}$ ), however all other kinetic parameters were consistent. Differences in values could be explained by variability between study populations, or use of arterial sampling of the blood input function and high-performance liquid chromatography for the metabolite correction in Becker et al., instead of an IDIF and literature values for corrections of the input function in our study. Relatively higher tracer delivery,  $K_1$ , could also be due to the higher temporal framing provided by the high sensitivity of EXPLORER (i.e., short 2-second framing compared to slower sampling in previous studies) [34]. For example, Fig. 7 from Volpi et al. demonstrates the effect of higher resolution 2s framing can lead to a higher peak for IDIFs and various regional TACs compared to lower resolution 10s framing [35].

In the present study, we measured quantitative amyloid in target and reference tissues, and the 2TCM was used to describe tracer kinetics in both regions. Kinetic modeling may be more accurate in cases where the cerebellum is not appropriate as a reference region, such as in familial AD that exhibits the presence of  $\beta$ -amyloid plaques in the cerebellum [36]. Future work could compare quantitative parameters in alternative reference regions such as whole cerebellum, white matter brain stem/pons, whole brainstem, and eroded subcortical white matter, which have shown good correlations with the gold standard plasma input-based quantification [37].

High quality kinetics and descending aorta IDIFs in this work were enabled by the uEXPLORER total-body PET/CT scanner which has a 194 cm axial field of view and a very high detection sensitivity [13]. Although SUVR is still clinically useful and is a simple and effective way of quantifying amyloid, quantification with kinetic modeling can achieve multiple kinetic parameters and reduce overestimation bias in SUVR, which is a limitation of SUVR despite its shorter scan time. In addition to perfusion, we also aim to continue acquiring dynamic scans for research purposes to investigate amyloid signal and links across different organs in the body in AD pathogenesis similar to other studies of cancer that have been done with uEXPLORER [38].

Comprehensive quantification of amyloid PET has many applications for future clinical use, especially in the context of improving early diagnosis, therapeutic intervention, and secondary prevention. Diagnostic decisions are often based on clinical reads of static SUVR, which does not reflect amyloid load as a continuous process. Absolute quantification can highlight specific pathological changes at early stages of AD, both in amyloid and perfusion, which has a direct impact on enrolling subjects and establishing an optimal window for therapeutic intervention. In addition, quantification is used to monitor treatment in clinical trials; has been shown to change diagnosis, patient management, and predict cognitive decline [39]; and is enabled by non-invasive methodology as presented in this work.

There were several limitations to this study. Metabolite fraction correction in the present study was based on a population average from Patt et al. to avoid invasive blood sampling [21]. Variability across individuals may be present in metabolite correction particularly at later time points, due to fast metabolism of  $^{18}F$ -labeled amyloid tracers, which can lead to partially inaccurate extraction fractions from kinetic modeling [40]. Variability due to metabolite correction can be further exaggerated as blood delivery varies between subjects and disease group, especially since aging and AD is linked to changes hepatic function and therefore the amount of radiometabolites [14]. On the contrary, Patt et al., found no significant difference between AD patients and healthy controls for both  $^{18}F$ -florbetaben metabolic profile, suggesting that applying the same metabolite fraction to both healthy and AD population, as done in our study, may still result in relatively low variability [21]. Nonetheless, applying a single population-based metabolite correction to two different populations may introduce additional statistical variability in our parameter estimates [14]. The true metabolite fraction estimation of our cohort may differ in this study despite similarities in the cohort of subjects. Individualized radiometabolite correction remains an unsolved challenge. Although previous studies have attempted to derive metabolite-free arterial input functions through the simultaneous estimation method (SIME) [41], estimation of tracer metabolism from multiple organ kinetics in a dynamic whole-body scan could be a future direction [42, 43]. Total-body imaging uEXPLORER, may allow for development of whole-body physiological model of radiotracer metabolism, which would allow more accurate estimation of IDIF without needing information from separate populations or arterial sampling [35]. In addition, directly comparing acquired arterial blood sampling with an IDIF could have further supported IDIF-based kinetics as a non-invasive alternative but was not within the scope of the study. The number of subjects included in this initial study

was relatively small, which we mitigate by leveraging the large amount of kinetic information across multiple brain regions in mixed-effects models. Our small sample with relatively few amyloid-positive cases made it difficult to directly evaluate the quantitative outcome measures ( $V_T$ ,  $V_s$ ) with  $BP_{ND}$ , which will be addressed with larger samples in future studies. As our focus was amyloid quantification with IDIF, reference-tissue based kinetic modeling (e.g., estimation of distribution volume ratios) were outside the scope of the present study but may be included in future work as another amyloid measure [20].

## Conclusion

The total-body EXPLORER PET allows for high quality, dynamic kinetic modeling of the whole body. Absolute quantification of  $\beta$ -Amyloid and multiple kinetic rate parameters from total-body  $^{18}\text{F}$ -florbetaben dynamic PET is feasible using a descending aorta IDIF. These two aspects enable non-invasive acquisition of accurate and quantitative measures of amyloid accumulation in clinical research of aging and dementia.

## Supplementary Information

The online version contains supplementary material available at <https://doi.org/10.1186/s13550-024-01104-7>.

Supplementary Material 1

Supplementary Material 2

Supplementary Material 3

Supplementary Material 4

## Acknowledgements

We would like to thank all the research volunteers who participated in this study. We are also grateful for the UC Davis Alzheimer Disease Research Center (ADRC), Life Molecular Imaging, and the EXPLORER Molecular Imaging Center. (EMIC) staff for their technical assistance.

## Author contributions

EH wrote the manuscript, performed all data evaluation, and statistical analysis. EH and AF conceived of the review and coordinated in its design. EL provided valuable guidance regarding kinetic modeling. AB assisted in the implementation of coregistration techniques. EF contributed the whole brain DKT atlas segmentations. DH provided valuable intellectual advice on appropriate models used for statistical analysis. BS performed image reconstruction. ERA provided patient demographics. SC, CD, and AF reviewed the manuscript and supported the conception of this review. All authors read and approved the final manuscript.

## Funding

NIH grant P30-AG072972 for the UC Davis Alzheimer's Disease Research Center and a generous gift from the Lena Bainer Alzheimer Research Fund.

## Data availability

The datasets generated during and analysed during the current study are available from the corresponding author on reasonable request.

## Declarations

### Ethics approval and consent to participate

The UC Davis Institutional Review Board approved this protocol and written informed consent was obtained for all subjects involved in the study. All procedures performed in studies involving human participants were in accordance with the ethical standards of the institutional and/or national research committee and with the 1964 Helsinki declaration.

### Consent for publication

Consent to publish has been received from all participants.

### Competing interests

No potential conflicts of interest relevant to this article exist.

Received: 20 December 2023 / Accepted: 2 March 2024

## References

1. Bao W, Xie F, Zuo C, Guan Y, Huang YH. PET neuroimaging of Alzheimer's Disease: Radiotracers and their utility in Clinical Research. *Front Aging Neurosci.* 2021;13:624330. <https://doi.org/10.3389/fnagi.2021.624330>.
2. Delrieu J, Bateman RJ, Touchon J, Sabbagh M, Cummings J. The future of AD clinical trials with the Advent of Anti-amyloid therapies: an CTAD Task Force Report. *J Prev Alzheimers Dis.* 2022;9(3):393–9. <https://doi.org/10.14283/jpad.2022.48>.
3. Choi WH, Um YH, Jung WS, Kim SH. Automated quantification of amyloid positron emission tomography: a comparison of PMOD and MIMneuro. *Ann Nucl Med.* 2016;30(10):682–9. <https://doi.org/10.1007/s12149-016-1115-6>.
4. Bullich S, Seibyl J, Catafau AM, et al. Optimized classification of 18F-Florbetaben PET scans as positive and negative using an SUVR quantitative approach and comparison to visual assessment. *NeuroImage Clin.* 2017;15:325–32. <https://doi.org/10.1016/j.nicl.2017.04.025>.
5. Heeman F, Yaqub M, Hendriks J, et al. Parametric imaging of dual-time window [18F]flutemetamol and [18F]florbetaben studies. *NeuroImage.* 2021;234:117953. <https://doi.org/10.1016/j.neuroimage.2021.117953>.
6. Heeman F, Yaqub M, Lopes Alves I, et al. Optimized dual-time-window protocols for quantitative [18F]flutemetamol and [18F]florbetaben PET studies. *EJNMMI Res.* 2019;9(1):32. <https://doi.org/10.1186/s13550-019-0499-4>.
7. Sabri O, Seibyl J, Rowe C, Barthel H. Beta-amyloid imaging with florbetaben. *Clin Transl Imaging.* 2015;3(1):13–26. <https://doi.org/10.1007/s40336-015-0102-6>.
8. Innis RB, Cunningham VJ, Delforge J, et al. Consensus nomenclature for in vivo imaging of reversibly binding radioligands. *J Cereb Blood Flow Metab off J Int Soc Cereb Blood Flow Metab.* 2007;27(9):1533–9. <https://doi.org/10.1038/sj.jcbfm.9600493>.
9. Heeman F, Yaqub M, Lopes Alves I, et al. Simulating the effect of cerebral blood flow changes on regional quantification of [18F]flutemetamol and [18F]florbetaben studies. *J Cereb Blood Flow Metab.* 2021;41(3):579–89. <https://doi.org/10.1177/0271678X20918029>.
10. Morris ED, Endres CJ, Schmidt KC, Christian BT Jr, Fisher RFM. RE. Kinetic Modeling in Positron Emission Tomography.
11. Cobelli CC. Introduction to modeling in Physiology and Medicine. 2nd ed. London: Elsevier/Academic; 2019.
12. Cherry SR, Badawi RD, Karp JS, Moses WW, Price P, Jones T. Total-body imaging: transforming the role of positron emission tomography. *Sci Transl Med.* 2017;9(381):eaaf6169. <https://doi.org/10.1126/scitranslmed.aaf6169>.
13. Spencer BA, Berg E, Schmall JP, et al. Performance evaluation of the uEXPLORER Total-Body PET/CT scanner based on NEMA NU 2-2018 with additional tests to characterize PET scanners with a long Axial Field of View. *J Nucl Med off Publ Soc Nucl Med.* 2021;62(6):861–70. <https://doi.org/10.2967/jnumed.120.250597>.
14. Zanotti-Fregonara P, Chen K, Liow JS, Fujita M, Innis RB. Image-derived input function for brain PET studies: many challenges and few opportunities. *J Cereb Blood Flow Metab.* 2011;31(10):1986–98. <https://doi.org/10.1038/jcbfm.2011.107>.
15. Cho SH, Shin JH, Jang H, et al. Amyloid involvement in subcortical regions predicts cognitive decline. *Eur J Nucl Med Mol Imaging.* 2018;45(13):2368–76. <https://doi.org/10.1007/s00259-018-4081-5>.

16. Badawi RD, Shi H, Hu P, et al. First Human Imaging Studies with the EXPLORER Total-Body PET Scanner\*. *J Nucl Med*. 2019;60(3):299–303. <https://doi.org/10.2967/jnumed.119.226498>.
17. Wang G, Nardo L, Parikh M, et al. Total-body PET multiparametric imaging of Cancer using a Voxelwise Strategy of Compartmental modeling. *J Nucl Med off Publ Soc Nucl Med*. 2022;63(8):1274–81. <https://doi.org/10.2967/jnumed.121.262668>.
18. Nardo L, Abdelhafez YG, Spencer BA, Badawi RD. Clinical implementation of total-body PET/CT at University of California, Davis. *PET Clin*. 2021;16(1):1–7. <https://doi.org/10.1016/j.cpet.2020.09.006>.
19. Committe for Medicinal Products for Human Use (CHMP). Florbetaben (18F). Published Online Dec 19, 2013.
20. Becker GA, Ichise M, Barthel H, et al. PET quantification of 18F-florbetaben binding to  $\beta$ -amyloid deposits in human brains. *J Nucl Med off Publ Soc Nucl Med*. 2013;54(5):723–31. <https://doi.org/10.2967/jnumed.112.107185>.
21. Patt M, Schildan A, Barthel H, et al. Metabolite analysis of [18F]Florbetaben (BAY 94-9172) in human subjects: a substudy within a proof of mechanism clinical trial. *J Radioanal Nucl Chem*. 2010;284(3):557–62. <https://doi.org/10.1007/s10967-010-0514-8>.
22. Smith SM. Fast robust automated brain extraction. *Hum Brain Mapp*. 2002;17(3):143–55. <https://doi.org/10.1002/hbm.10062>.
23. Jenkinson M, Smith S. A global optimisation method for robust affine registration of brain images. *Med Image Anal*. 2001;5(2):143–56. [https://doi.org/10.1016/s1361-8415\(01\)00036-6](https://doi.org/10.1016/s1361-8415(01)00036-6).
24. Jenkinson M, Bannister P, Brady M, Smith S. Improved optimization for the Robust and Accurate Linear Registration and Motion correction of brain images. *NeuroImage*. 2002;17(2):825–41. <https://doi.org/10.1006/nimg.2002.1132>.
25. Klein A, Tourville J. 101 Labeled Brain Images and a Consistent Human Cortical Labeling Protocol. *Front Neurosci*. 2012;6. Accessed June 21, 2023. <https://www.frontiersin.org/articles/https://doi.org/10.3389/fnins.2012.00171>.
26. Feng T, Zhao Y, Shi H, et al. Total-body quantitative Parametric Imaging of Early Kinetics of 18F-FDG. *J Nucl Med off Publ Soc Nucl Med*. 2021;62(5):738–44. <https://doi.org/10.2967/jnumed.119.238113>.
27. Benjamini Y, Hochberg Y. Controlling the false Discovery rate: a practical and powerful Approach to multiple testing. *J R Stat Soc Ser B Methodol*. 1995;57(1):289–300. <https://doi.org/10.1111/j.2517-6161.1995.tb02031.x>.
28. R Core Team. (2021). R: A language and environment for statistical computing. R Foundation for Statistical Computing, Vienna, Austria. <https://www.R-project.org/>.
29. Palmqvist S, Schöll M, Strandberg O, et al. Earliest accumulation of  $\beta$ -amyloid occurs within the default-mode network and concurrently affects brain connectivity. *Nat Commun*. 2017;8(1):1214. <https://doi.org/10.1038/s41467-017-01150-x>.
30. Ebenau JL, Visser D, Verfaillie SCJ, et al. Cerebral blood flow, amyloid burden, and cognition in cognitively normal individuals. *Eur J Nucl Med Mol Imaging*. 2023;50(2):410–22. <https://doi.org/10.1007/s00259-022-05958-8>.
31. Su Y, Blazey TM, Snyder AZ, et al. Quantitative amyloid imaging using image-derived arterial input function. *PLoS ONE*. 2015;10(4):e0122920. <https://doi.org/10.1371/journal.pone.0122920>.
32. Li E, Cherry S, Tarantal A, et al. Identification and comparison of image-derived input functions using total-body PET. *J Nucl Med*. 2019;60(supplement 1):520–520.
33. Zhang X, Cherry SR, Xie Z, Shi H, Badawi RD, Qi J. Subsecond total-body imaging using ultrasensitive positron emission tomography. *Proc Natl Acad Sci*. 2020;117(5):2265–7. <https://doi.org/10.1073/pnas.1917379117>.
34. Girard A, Saint-Jalmes H, Chaboub N, et al. Optimization of time frame binning for FDOPA uptake quantification in glioma. *PLoS ONE*. 2020;15(4):e0232141. <https://doi.org/10.1371/journal.pone.0232141>.
35. Volpi T, Maccioni L, Colpo M, et al. An update on the use of image-derived input functions for human PET studies: new hopes or old illusions? *EJNMMI Res*. 2023;13(1):97. <https://doi.org/10.1186/s13550-023-01050-w>.
36. Catafau AM, Bullich S, Seibyl JP, et al. Cerebellar Amyloid- $\beta$  plaques: how frequent are they, and do they influence 18F-Florbetaben SUV ratios? *J Nucl Med off Publ Soc Nucl Med*. 2016;57(11):1740–5. <https://doi.org/10.2967/jnumed.115.171652>.
37. Heeman F, Hendriks J, Lopes Alves I, et al. [11 C]PIB amyloid quantification: effect of reference region selection. *EJNMMI Res*. 2020;10:123. <https://doi.org/10.1186/s13550-020-00714-1>.
38. Wang Y, Nardo L, Spencer B, et al. Multi-organ metabolic changes in COVID-19 recovery measured with total-body dynamic 18F-FDG PET. *J Nucl Med*. 2022;63(supplement 2):2329–2329.
39. Pemberton HG, Collij LE, Heeman F, et al. Quantification of amyloid PET for future clinical use: a state-of-the-art review. *Eur J Nucl Med Mol Imaging*. 2022;49(10):3508–28. <https://doi.org/10.1007/s00259-022-05784-y>.
40. Nelissen N, Laere KV, Thurfjell L, et al. Phase 1 study of the Pittsburgh compound B derivative 18F-Flutemetamol in healthy volunteers and patients with probable Alzheimer Disease. *J Nucl Med*. 2009;50(8):1251–9. <https://doi.org/10.2967/jnumed.109.063305>.
41. Sari H, Erlandsson K, Marner L, et al. Non-invasive kinetic modelling of PET tracers with radiometabolites using a constrained simultaneous estimation method: evaluation with 11 C-SB201745. *EJNMMI Res*. 2018;8:58. <https://doi.org/10.1186/s13550-018-0412-6>.
42. Hardiansyah D, Guo W, Kletting P, Mottaghy FM, Glatting G. Time-integrated activity coefficient estimation for radionuclide therapy using PET and a pharmacokinetic model: a simulation study on the effect of sampling schedule and noise. *Med Phys*. 2016;43(9):5145–54. <https://doi.org/10.1118/1.4961012>.
43. Bartelink IH, van de Stadt EA, Leeuwerik AF, et al. Physiologically based pharmacokinetic (PBPK) modeling to Predict PET Image Quality of three generations EGFR TKI in Advanced-Stage NSCLC patients. *Pharmaceuticals*. 2022;15(7):796. <https://doi.org/10.3390/ph15070796>.

## Publisher's Note

Springer Nature remains neutral with regard to jurisdictional claims in published maps and institutional affiliations.